LAWRENCE
LIVERMORE
NATIONAL
LABORATORY

LLNL-TR-411038

Active Detection and Imaging of Nuclear Materials with High-Brightness Gamma Rays

C. P. J. Barty, D. J. Gibson, F. Albert, S. G. Anderson, G. G. Anderson, S. M. Betts, R. D. Berry, S. E. Fisher, C. A. Hagmann, M. S. Johnson, M. J. Messerly, H. H. Phan, V. A. Semenov, M. Y. Shverdin, A. M. Tremaine, F. V. Hartemann, C. W. Siders, D. P. McNabb

March 4, 2009

Disclaimer

This work performed under the auspices of the U.S. Department of Energy by Lawrence Livermore National Laboratory under Contract DE-AC52-07NA27344.

FY08 LDRD Final Report

Active Detection and Imaging of Nuclear Materials with High-Brightness Gamma Rays

LDRD Project Tracking Code: 06-SI-002

Christopher P. J. Barty, Principal Investigator

Report Co-authors: David Gibson, Felicie Albert, Scott Anderson, Gerry Anderson, Shawn Betts, Robert Berry, Scott Fisher, Christian Hagmann, Micah Johnson, Mike Messerly, Henry Phan, Vladimir Semenov, Miro Shverdin, Aaron Tremaine, Fred Hartemann, Craig Siders, Dennis McNabb, and Chris Barty.

Abstract

A Compton scattering γ-ray source, capable of producing photons with energies ranging from 0.1 MeV to 0.9 MeV has been commissioned and characterized, and then used to perform nuclear resonance fluorescence (NRF) experiments. The performances of the two laser systems (one for electron production, one for scattering), the electron photoinjector, and the linear accelerator are also detailed, and γ-ray results are presented. The key source parameters are the size (0.01 mm^2), horizontal and vertical divergence (6×10 $mrad^2$), duration (10 ps), spectrum and intensity (10^5 photons/shot). These parameters are summarized by the peak brightness, 1.5×10^{15} photons/mm^2/$mrad^2$/s/0.1%bandwidth, measured at 478 keV. Additional measurements of the flux as a function of the timing difference between the drive laser pulse and the relativistic photoelectron bunch, γ-ray beam profile, and background evaluations are presented. These results are systematically compared to theoretical models and computer simulations. NRF measurements performed on ^{7}Li in LiH demonstrate the potential of Compton scattering photon sources to accurately detect isotopes *in situ*.

I. INTRODUCTION

Over the past two decades, considerable technological improvements in the field of high intensity lasers, high brightness electron linacs, and x-ray diagnostics have contributed to the maturation of a novel type of light sources based on Compton scattering, where incident laser photons are scattered and Doppler upshifted by a relativistic electron beam to generate tunable, highly collimated, ps-fs photon flashes, with relatively narrow spectral bandwidth.

Concurrently, an increasing number of important applications are being explored, either experimentally, or via detailed computer simulations. At photon energies below 100 keV, advanced biomedical imaging techniques, including ultrafast x-ray protein crystallography [1], phase contrast imaging [2], and K-edge imaging [3], are under consideration by a number of groups worldwide. Although synchrotron light sources [4] and x-ray free-electron lasers such as LCLS [5] or the European XFEL [6] can produce x-rays at higher brightness in this energy range, Compton scattering light sources are attractive because of their compact footprint. At photon energies relevant for nuclear processes and applications, these new radiation sources will produce the highest beam fluxes. Applications include Nuclear Resonance Fluorescence (NRF) [7], picosecond positron beams [8], and photo fission. It is already the case with HIγS [9], a large 1-86 MeV high intensity γ-ray facility producing polarized photons via intra-cavity Compton backscattering in a free electron laser, that has already been used as a research tool to assign the parity of excited states in nuclei using NRF [10].

The detection of low-Z, low-density objects shielded by high-Z, dense material is a long-standing problem that has important applications ranging from homeland security and non-proliferation [11] to advanced biomedical imaging and paleontology. X-rays are sensitive to electron density and x-ray radiography yields poor contrast in these situations. NRF offers a unique approach to the so-called inverse density radiography problem. NRF is a process in which nuclei are excited by discrete high-energy (typically MeV) photons and subsequently re-emit γ-rays at discrete energies determined by the structure of the nucleus. Because the resonance structure is determined by the number of neutrons and protons present in the nucleus, NRF can provide isotope specific detection and imaging capability [7]. NRF has been recently used to detect shielded, dense, high-Z materials, such as ^{235}U or ^{239}Pu, with a 4 MeV bremsstrahlung source [12].

NRF transitions are narrow band ($\Delta E/E \simeq 10^{-6}$); thus monochromatic Compton-

scattering sources are favorable for that type of application when compared with Bremsstrahlung sources. Since Bremsstrahlung sources have 100% bandwidth, they create considerable background via elastic Compton scattering and other processes. Furthermore, the dose required for detection is much higher than for a Compton source. Recently, ^{208}Pb has been detected in an iron box by using γ-rays produced by the collision of a Q-switched laser beam and a high energy electron beam from a storage ring [13].

This report is organized as follows: in the remainder of this section, properties of Compton backscattering sources as well as relevant theoretical considerations are presented, which also forms the basis of the computer codes used to analyze the data. In Section II, the hardware systems built are presented and characterized in detail. Section III reviews the full characteristics of the photon beam, such as its spatial and spectral information. Comparisons with theory are provided throughout the analysis of our data. Finally, Section IV presents the results of experiments to detect NRF from ^{7}Li as an application of this source.

A. Properties of Compton scattering sources

Compton scattering sources' properties, which have been extensively studied [14–18], rely on energy-momentum conservation. With this feature, one can derive the relativistic Doppler shifted energy:

$$E_x = \frac{2\gamma^2(1-\cos\phi)}{1+\gamma^2\theta^2+2\gamma k_0\lambda_c}E_L, \tag{1}$$

where γ is the electron relativistic factor, ϕ is the angle between the incident laser and electron beams, $k_0 = 2\pi/\lambda$ is the laser wavenumber, $\lambda_c = 2.426\times10^{-12}$ m is the Compton wavelength, and E_L is the laser energy. The electron recoil, $2\gamma k_0\lambda_c$, is a few 10^{-3} for our experimental parameters ($\gamma \simeq 200$, $k_0 \simeq 10^7$) and can therefore be neglected. And in the case of a head-on collision ($\phi = 180°$), the scattered energy roughly scales as $4\gamma^2 E_L$. This makes Compton scattering sources very attractive because one can obtain high-energy (MeV) scattered photons with relatively modest electron beam energies, making the source rather compact compared to machines like 3^{rd} generation synchrotrons [4]. An important feature of Compton scattering sources is that the Compton scattering cross-section is very small ($\sigma = 6.65\times10^{-25}$ cm^2), so a high density of electrons and photons (and thus very high-quality beams) are required at the interaction point. In the case where the laser focal spot and electron bunch focus have similar size, w_0, the number of X-rays produced can

be approximated by $N_x = (\sigma/\pi w_0^2) N_L N_e$, where N_L and N_e are respectively the number of laser photons and the number of electrons in the bunch. As the electron beam focal spot size scales as $1/\gamma$, the X-ray yield varies as γ^2. While typical synchrotrons provide the highest brightness in the 10-100 keV range, Compton scattering sources become a more efficient option at higher energies. Besides their energy-angle correlation and brightness at high energies, Compton scattering sources are attractive because they are highly collimated.

B. Modelling

1. Normalized spectrum

The computer code used to analyze the data considers Compton scattering by electrons with a given phase space distribution interacting with a Gaussian-paraxial electromagnetic wave, but neglecting wavefront curvature. This is adequate for laser foci with sufficiently large (> 10) F-numbers ($= 1.22\lambda f/D$, where f is the focal length, D the beam diameter, and λ the laser wavelength). The key quantities used in our analysis and a detailed description of the formalism used here can be found in Ref. [19]. We first calculate the Compton scattering frequency by utilizing the energy-momentum conservation law:

$$\kappa - \lambda = \lambda_c (k_\mu q^\mu), \tag{2}$$

where $\lambda_c = \hbar/m_0 c$ is the Compton wavelength of the electron, κ and λ are the incident and scattered light cone variables, $k_\mu = (k, 0, 0, 0, k)$ is the incident laser pulse 4-wavenumber and q_μ is the scattered 4-wavenumber. By solving this equation for q, one obtains the relativistic Doppler shift and recoil:

$$q_c = \frac{k(\gamma - u_z)}{\gamma - u_z \cos\theta + k\lambda_c(1 - u_x \sin\theta\cos\phi - u_y \sin\theta \sin\phi - u_z \cos\theta)}, \tag{3}$$

where θ and ϕ refer to the classical spherical coordinates (in the case of a counter-propagating scheme $\theta = \pi$ and $\phi = 0$) and where $u_\mu = (\gamma = \sqrt{1 + u_x^2 + u_y^2 + u_z^2}, u_x, u_y, u_z)$ is the electron 4-vector and γ its relativistic factor. From there, one can generate a random normal distribution of particles with positions u_x, u_y and relativistic factor γ and standard deviations $\Delta u_x = j\epsilon_x/\sigma_x$, $\Delta u_y = j\epsilon_y/\sigma_y$ and Δ_γ respectively. The quantities ϵ and σ refer to the electron beam normalized emittance and spot size and j to the jitter. One then obtains as many values of q_c (ranging from q_{cmin} to q_{cmax}) as particles used in the code that can

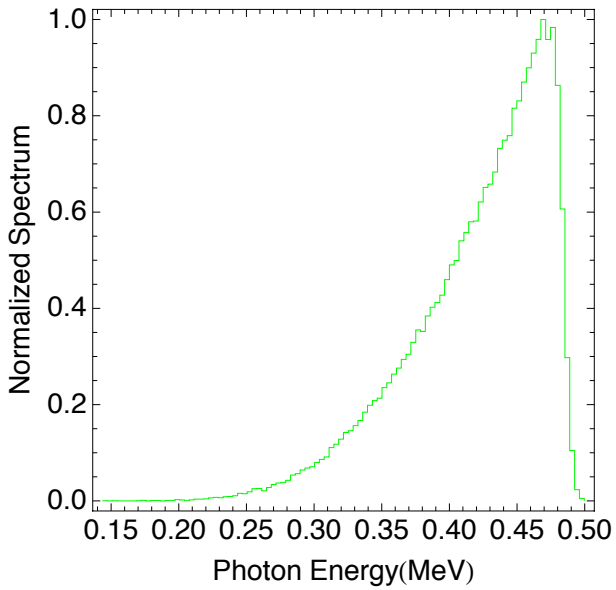

FIG. 1: Example of a spectrum simulated with Mathematica, using 100000 particles and 100 bins for an electron beam energy of 116 MeV and a laser wavelength of 532 nm (energy 2.33 eV). The other parameters are $j = 2$, $\epsilon_x = 5$ mm mrad, $\epsilon_y = 6$ mm mrad, $\sigma_x = 35$ μm and $\sigma_y = 40$ μm.

be sampled over a number n of bins of width $q_{bin} = (q_{cmax} - q_{cmin})/n$. Figure 1 gives an example of a normalized spectrum obtained with this code.

2. Dose

To calculate the total integrated number of γ-ray photons and their spectral distribution yielded by the interaction, one has to take into account several other parameters. The most useful expression to describe the source is typically the local differential brightness, which can be derived from the local number of photons scattered per unit time and volume [20]:

$$\frac{d^{12}N}{d^4x d\Omega dq d^3u d^3k} = \frac{d\sigma}{d\Omega}\delta(q - q_c)\frac{d^3n_e}{d^3u}\frac{d^3n_\lambda}{d^3k}\frac{u_\mu k^\mu}{\gamma k}, \tag{4}$$

where d^3n_e/d^3u and d^3n_λ/d^3k represent the electron beam and laser pulse phase space densities.

We start with the differential scattering cross-section $d\sigma/d\Omega$ described by the Lorentz-boosted Klein-Nishina formula, as derived by Bhatt et al. [21], in which we only use the

spin-independent component:

$$\frac{d\sigma}{d\Omega} = \frac{1}{2}(\alpha\lambda_c)^2 \left(\frac{q}{\kappa}\right)^2 \left[\frac{1}{2}\left(\frac{\kappa}{\lambda}+\frac{\lambda}{\kappa}\right) - 1 + 2\left(\epsilon_\mu\pi^\mu - \frac{(\epsilon_\mu u^\mu)(\pi_\nu v^\nu)}{\kappa\lambda_c} + \frac{(\epsilon_\mu v^\mu)(\pi_\nu u^\nu)}{\lambda\lambda_c}\right)^2\right], \quad (5)$$

where α is the fine structure constant, $\epsilon_\mu = (0,1,0,0,0)$ corresponds to a linearly polarized incident radiation and π_μ is the scattered 4-polarization. $v_\mu = u_\mu + \lambda_c(k_\mu - q_\mu)$ is the 4-velocity after the scattering event. The polarization state can be defined by constructing two orthogonal unit vectors that are both perpendicular to the direction of observation and the cross-section is averaged over the scattering polarization angle.

In the case of a single electron following a trajectory $\mathbf{r}(\tau)$, where τ is its proper time, the phase space density is given by a product of Dirac delta-distributions:

$$\frac{d^3n_e}{d^3u} = \delta[\mathbf{x}-\mathbf{r}(\tau)]\delta[\mathbf{u}-\mathbf{u}(\tau)] = \delta[\mathbf{x}-\mathbf{r}(\tau)]\delta\left[\mathbf{u}-\frac{d\mathbf{r}(\tau)}{cd\tau}\right], \quad (6)$$

and thus, after integration over all the electron phase space, the brightness reads:

$$\frac{d^3N}{cdtd\Omega dq} = \iiint_{\mathbb{R}^3} \frac{d\sigma}{d\Omega}\delta(q-q_c)\frac{d^3n_\lambda}{d^3k}[\mathbf{r}(\tau),\tau]\frac{u_\mu(\tau)}{\gamma(\tau)}\frac{k^\mu}{k}d^3k. \quad (7)$$

In the case of an uncorrelated incident photon phase space, corresponding to the Fourier transform limit, the phase space density takes the form of a product,

$$\frac{d^3n_\lambda}{d^3k} = n_\lambda(x_\mu)\widetilde{n}_\lambda(k_\nu); \quad (8)$$

the number of photons scattered per unit wavenumber and solid angle is then given by:

$$\frac{d^2N}{d\Omega dq} = \int_{-\infty}^{\infty} n_\lambda[\mathbf{r}(\tau),\tau]cdt \iiint_{\mathbb{R}^3} \frac{d\sigma}{d\Omega}\delta(q-q_c)\widetilde{n}_\lambda(k_\nu)\frac{\kappa}{\gamma k}d^3k. \quad (9)$$

In our analysis, we consider the case of a plane wave in the Fourier domain:

$$k_x = k_y = 0, k_z = k, \widetilde{n}_\lambda = \frac{\exp[-(\frac{k-k_0}{\Delta k})^2]}{\sqrt{\pi}\Delta k}. \quad (10)$$

The integral over k is easily performed by using the fact that:

$$\delta[f(x)] = \sum \frac{\delta(x-x_n)}{|f'(x_n)|}, \quad (11)$$

where x_n represents the poles of the function f. Applying this rule to our case, we first look for the poles k_p of q_c by solving for $q_c(k)$=0, and using the above in (9), we find:

$$\frac{d^2N}{d\Omega dq} = \frac{1}{\sqrt{\pi}\Delta k}\left[\frac{d\sigma}{d\Omega}\frac{\kappa}{\gamma k}\frac{e^{-(k-k_0)^2/\Delta k^2}}{|\partial_k q_c(k)|}\right]_{k=k_p} \int_{-\infty}^{\infty} n_\lambda[\mathbf{r}(\tau),\tau]cdt \quad (12)$$

For a Gaussian laser pulse, the incident photon density can be modeled analytically within the paraxial approximation, and in the case of a cylindrical focus:

$$n_\lambda(\mathbf{x},t) = \frac{N_\lambda}{\sqrt{\pi/2}^3 w_0^2 c\Delta t}\frac{1}{1+(z/z_0)^2}\exp\left[-2\left(\frac{t-z/c}{\Delta t}\right)^2 - 2\frac{r^2}{w_0^2[1+(z/z_0)^2]}\right], \tag{13}$$

where N_λ is the total number of photons in the laser pulse, Δt the pulse duration, w_0 the $1/e^2$ focal radius and $z_0 = \pi w_0^2/\lambda_0$ is the Rayleigh range. To evaluate the integral in (12), we replace the spatial coordinates by the ballistic electron trajectory:

$$x(t) = x_0 + \frac{u_x}{\gamma}ct, y(t) = y_0 + \frac{u_y}{\gamma}ct, z(t) = z_0 + \frac{u_z}{\gamma}ct, r^2(t) = x^2(t) + y^2(t), \tag{14}$$

where we can divide x, y and r by w_0 and z and ct by z_0 to obtain the normalized quantities $\overline{x}$, $\overline{y}$, $\overline{z}$, $\overline{r}$ and $\bar{t}$. One finally obtains the expression:

$$\frac{d^2N}{d\Omega dq} = \frac{1}{\sqrt{\pi}\Delta k}\left[\frac{d\sigma}{d\Omega}\frac{\kappa}{\gamma k}\frac{e^{-(k-k_0)^2/\Delta k^2}}{|\partial_k q_c(k)|}\right]_{k=k_p}\frac{N_\lambda}{\sqrt{\pi/2}^3 w_0^2 c\Delta t} \int_{-\infty}^{\infty}\frac{1}{1+\overline{z}^2}\exp\left[-2\left(\frac{z_0}{c\Delta t}\right)^2(\bar{t}-\overline{z})^2 - 2\frac{\overline{r}^2}{1+\overline{z}^2}\right]d\bar{t}. \tag{15}$$

We finally note that when evaluating (15) it is sufficient to calculate the integral within an interval of $\sim 10\Delta t$ as we assume a Gaussian temporal pulse profile.

II. THE γ-RAY SOURCE

The experiments have been performed at the LLNL 100 MeV linac facility, which is located in a well shielded environment, 10 meters below ground. An overview of the experimental facility is presented in Fig. 2. There were three main caves in which the experiments were made: the outer-detector cave, where the Interaction Laser System (ILS) was located, the accelerator cave, containing the photo-cathode and the Photoinjector drive laser (PDL), the linac and the interaction point, and finally the 0° cave, located 20 meters away from the interaction point, on the other side of a thick concrete wall where the γ-ray diagnostics, including germanium detectors, were setup.

Given the limited space and rf power available at the LLNL accelerator facility, we designed a machine to demonstrate NRF measurements by exciting the relatively low-energy lines at 478 keV for ^{7}Li and 680 keV for ^{238}U using $\sim$ 120 MeV electron energies and either 532 nm or 351 nm laser light. A block diagram of the complex system is shown in Fig. 3. It

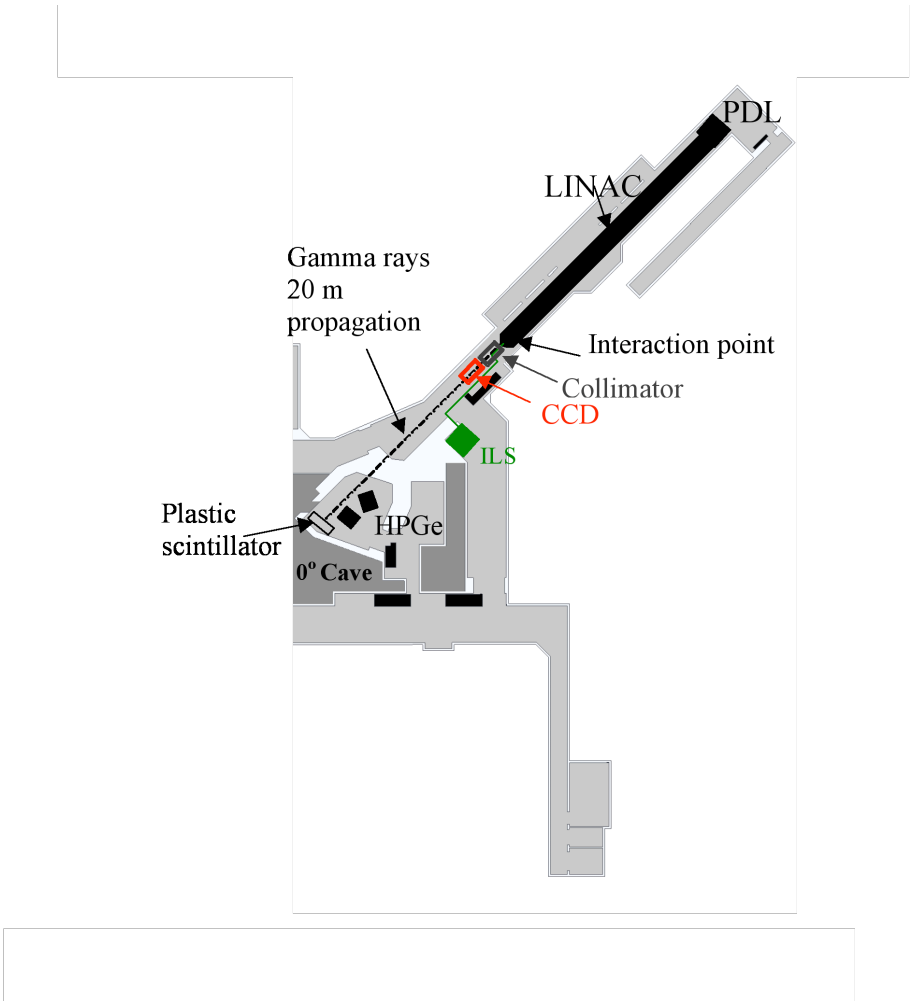

FIG. 2: Overview of the experimental facility with the outer-detector (laser) cave, the accelerator cave and the 0 degree cave.

consists of the laser components (two lasers with a common front end), the electron beam components (the photoinjector, linac, and rf source), and the interaction region where the scattering takes place, generating γ-rays. Each of these subsystems is described in detail below.

A. Laser Systems

The T-REX source requires two laser systems that are precisely synchronized: one to generate the electron beam at the photocathode (the "Photoinjector Drive Laser" or PDL), and one to scatter off the focused electron beam at the end of the linac (the"Interaction

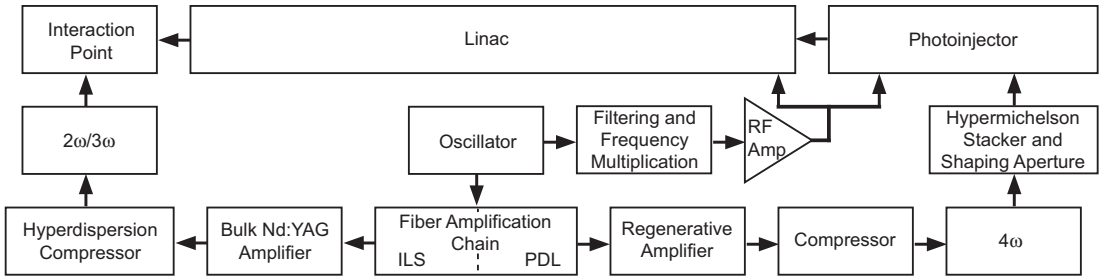

FIG. 3: A block diagram of the T-REX system, showing all the subcomponents described in detail in the text.

Laser System", or ILS). In order to ensure the synchronicity of the two lasers, they are seeded with the same fiber based oscillator. Both lasers have matching front ends that are all fiber based (collectively, the "Seed Laser System" or SLS), which then feed into the main PDL and ILS systems.

The SLS laser oscillator produces a 1053 nm pulse of 200 fs (8 nm bandwidth) and 200 pJ at a rate of 40.7785 MHz. This output then serves as the seed to the ILS and the PDL, in which the chirped pulse amplification technique (CPA) [22] is used. For both lasers, the pulse is stretched up to a few ns by using a chirped fiber bragg grating (CFBG) then amplified in a series of fiber amplifiers. Acousto-optic modulators slice the pulse train down to a 10 kHz reprate. After this amplification, the pulses, on the order of 1 μJ in energy, are coupled into a large mode-area photonic bandgap fiber, where the pulse are amplified to 50 μJ before being delivered to the PDL and ILS bulk amplification systems.

1. Photoinjector Drive Laser (PDL)

The energy delivered by the fiber seed isn't sufficient to drive the photocathode directly, so the pulse energy is boosted by a regenerative amplifier based upon the design for the National Ignition Facility [23]. The amplifier head consists of a Nd:Phosphate glass (Schott LG770) rod that is end-pumped by an 800nm laser diode array homogenized by a hollow duct concentrator. The amplifier was designed to operate at 10 Hz with an 18 ns round trip time. The diode pump power and number of round trips were adjusted to yield 1.5 mJ output pulses at peak buildup for maximum energy stability. A Pockels cell enabled Q-switched cavity-dumped operation.

After the regenerative amplifier, the pulse is recompressed with a transmission efficiency

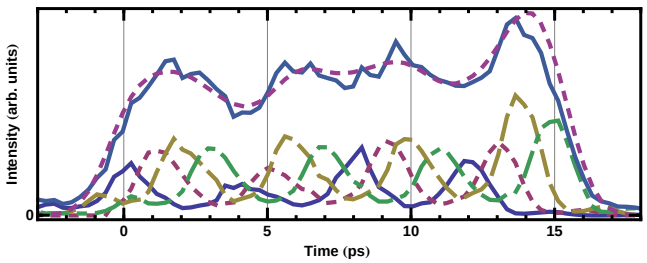

FIG. 4: Crosscorrelation of PDL stacked UV pulse with residual IR. The bottom traces show the sixteen individual pulses, and the upper traces show the sum of the crosscorrelations (solid curve) and the predicted shape based on gaussians of the measured width with the individually measured energies.

of 66%. The compressor grating is a 1740 l/mm dielectric grating at an incidence angle of 75°, with a translatable horizontal roof mirror to set the effective grating separation and a vertical roof mirror to offset the beam for extraction at the compressor exit. Following the compressor the pulse is frequency doubled to 527 nm with a 1.0 mm thick BBO crystal, then doubled again to 263 nm with a 0.45 mm thick BBO crystal, yielding a final energy of 100 μJ.

To minimize the contribution of space charge effects on the electron beam emittance, our target laser pulse shape is a uniform-intensity cylinder of photons, based on previous simulations of our photoinjector [24]. We have approximated the necessary temporal shape by stacking several short pulses together to minimize the rise and fall times of the beam. The frequency-quadrupled pulse is fed into a hyper-Michelson pulse stacker [25], which splits the pulse into 16 replicas through a series of four beam splitters. By sequencing the beam splitters correctly (using the two outputs (one with variable delay) of the first as two inputs to the second, etc.), rotating the polarization of one of the two final outputs with a waveplate, then combining the two outputs with a polarizer, no laser energy is wasted. Choosing the delays correctly allows adjacent pulses to have crossed polarizations, minimizing interference between the pulses which could lead to significant longitudinal ripple on the delivered pulse. Because we are illuminating the photocathode nearly on axis, the polarization of the laser light isn't significant.

The resulting temporal profile was measured two ways. First, the output of the stacker (4ω) was cross-correlated with the residual IR light (1ω) from the frequency conversion in

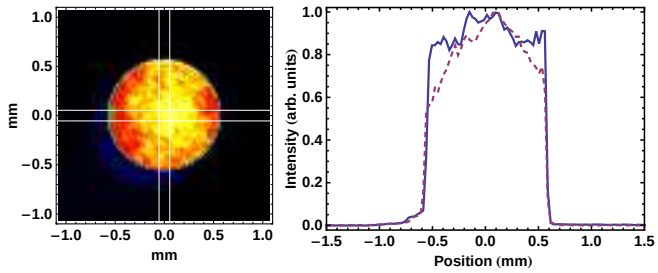

FIG. 5: Bottom: The apertured PDL profile (left), and averaged lineouts within the boxed regions (right - solid: vertical, dashed: horizontal).

a BBO crystal, resulting via difference frequency generation in a signal at 3ω. The pulses were measured in groups of four so they could be seen individually, and the results are shown at the bottom of Fig. 4. The gaussian width of the individual pulses is $\sigma = 0.83$ ps. This is consistent with an initial IR pulse width of $\sigma_{\rm ir} = 0.74$ ps and a UV pulse width of $\sigma_{\rm uv} = 0.37$ ps. Second, at the output of the hyper-Michelson stacker, the energy of each of the individual pulses was measured by selectively blocking the delay arms. Using this set of energies, coupled with the width measured in the cross-correlation, to define gaussian pulses to sum, the expected pulse shape is shown in the upper plot of Fig. 4 (dashed line). Scaling the cross correlation measurements based on the measured energy of the largest pulse in each group, then summing those four plots, we obtain the curve shown in the upper plot of Fig. 4 (solid line). The deviation from the target flat-topped shape is due to the uneven splitting ratio of the beamsplitters used — measurement of the transmission of each of the splitters predicts the energy distribution observed. This issue will be addressed in future designs.

To get the required transverse beam shape, the output of the hyper-Michelson stacker is clipped by a 1.2 mm diameter aperture. Although this method has the disadvantage of discarding a significant amount of laser light, it has the advantages of being both simple to implement and easy to modify (to allow optimization of the electron emittance). The gaussian beam size at the aperture is measured to be $\sigma_x = 0.61$ mm $\times$ $\sigma_y = 0.87$ mm, which means the 1.2 mm diameter aperture will pass only 28% of the laser energy. The aperture plane is relay imaged with a pair of 1 m focal length lenses, forming a 1:1 imaging telescope, to the cathode surface in the photoinjector. A small portion of the beam is picked off and sent to a camera sitting at an equivalent image plane (Fig. 5) and an energy meter. The

energy delivered to the photocathode is adjusted to get the desired operating charge, but a value of 17 ± 1 μJ is typical.

2. Interaction Laser System (ILS)

The design specifications for the ILS were chosen to optimize the scattering process that is fundamental to the Compton-source's operation. The number of scattering events an electron will experience is proportional to the column density of the photon field along the electron's direction of travel. To maximize the γ-ray flux, we want to maximize the column density, subject to two limiting factors. First, if the photon density becomes too high, nonlinear effects (multiple scattering events) start to dominate the scattering and significantly broaden the bandwidth of the source. To avoid this, we want to make the laser pulse as long as possible. Additionally, long pulses require less bandwidth in the laser spectrum, and laser bandwidth contributes linearly to γ-ray bandwidth (since $E_x \propto E_l$). The second limiting factor is the length over which the laser and electron beams are focused. At distances from the focal plane of the laser defined by the Rayleigh range

$$z_r = \frac{\pi w_0^2}{\lambda} \qquad\qquad w(z) = w_0 \sqrt{1 + \left(\frac{z}{z_r}\right)^2} \tag{16}$$

[where $w(z)$ is the $1/e^2$ intensity radius of the laser and $w_0 = w(0)$ corresponds to the laser focus], the beam diameter increases, causing the photon density (and therefore the scattering rate) to drop. For $w_0 = 40$ μm and $\lambda = 532$ñm wavelength z_r corresponds to a pulse length of $\sim$ 10sp̃s. Pulses longer than this means part of the interaction occurs away from the focus, so more laser energy per scattered photon is required. To get pulse lengths on the order of 10p̃s at $\lambda = 1$ μm wavelength requires a bandwidth 0.1 nm, which allows for the possibility of using commerical Nd:YAG technology, with has a gain bandwidth of $\Delta\lambda \approx 0.4$ nm, for amplification.

The ILS laser system starts with the fiber laser seed source discussed above, which supplies a 10 kHz train of 20 μJ pulses at 1064 nm with 1.3 nm bandwidth stretched to nominally 5 ns in the CFBG. This pulse duration is similar to that of commercial Q-switched Nd:YAG lasers. However, such commercial lasers are limited to a few longitudinal modes, as opposed to the relatively wide-spectrum chirped pulses that the fiber provides. Following the fiber seed is a three-head Nd:YAG power amplifier and a hyper-dispersion pulse compressor. The

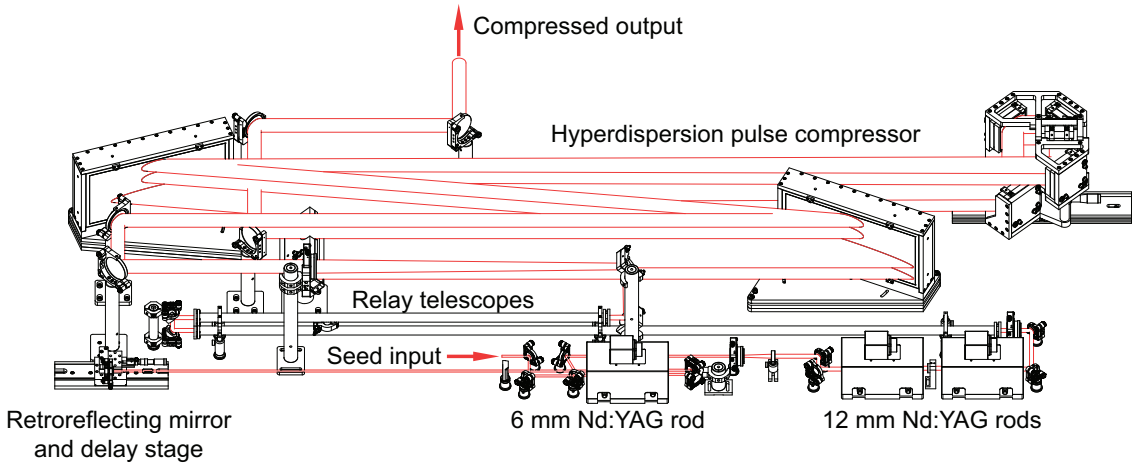

FIG. 6: Diagram showing the bulk ampifiers and compressor for the Interaction Laser System. The seed is sent though three Nd:YAG heads then relay imaged and upcollimated for injection into the hyper-dispersion pulse compressor.

beam after the compressor, initially at 1064 nm, can then be frequency doubled or tripled using large aperture DKDP crystals. The layout of the bulk amplifiers and the dispersion compressor is shown in Fig. 6.

The three-head Nd:YAG amplifier chain has been manufactured by Continuum and consists of laser heads and power supplies used in their Powerlite Plus laser. The first laser head contains two side-by-side 6 mm diameter Nd:YAG rods pumped by a single flashlamp. The second and third laser heads each consist of a 12 mm diameter Nd:YAG rod. A pockels cell before the amplifier slices out a 10 Hz pulse train from the fiber seed. The pulses then double pass each of the 6 mm rods and single pass each of the 12 mm rods. An expanding telescope doubles the beam size before the 12 mm rods. The spatial beam profile is Gaussian and the fill factor in the rods (20-25%) is kept small enough to minimize interference rings caused by beam clipping. Negative lenses placed after laser heads compensate for thermal focusing and a quartz half-wave rotator between the 12mm rods partially compensates for thermal birefringence. An adjustable delay stage after the first pass through the 6mm heads is used to control the relative timing between the laser pulses and the electron beam at the interaction point. The seed pulse energy is amplified to 1.2 J and the pulse bandwidth is gain narrowed from 1.3 nm FWHM in the seed pulse to 0.25 nm at the amplifier output.

For pulse compression, we use a novel hyper-dispersion grating compressor. Chirped-pulse amplification in Nd:YAG with sub-nanometer bandwidths is impractical using traditional

two-grating pulse compressors due to exceedingly large grating spacing ($\sim$ 25 m with 1740 grooves/mm gratings). We use a cascaded "hyper-dispersion" architecture to provide the necessary dispersion (7100 ps/nm) in a compact meter-scale compressor. Our design uses four multi-layer dielectric (MLD) diffraction gratings in a double-pass configuration. The use of MLD gratings allows for high throughput efficiency in the compressor despite a total of eight grating reflections. The beam is incident at 3° off the Littrow angle on all of the 1740 g/mm gratings. The first grating angularly disperses the incident collimated beam, and the second grating is arranged anti-parallel to the first and further disperses the already dispersed beam. The third and fourth gratings are arranged parallel, respectively, to the second and first gratings to collimate the spatially chirped beam. To simplify multi-grating alignment and reduce grating cost, we fold the beam path to reduce to two the total number of gratings. The chosen grating dimensions are 40×20 cm^2, determined by the total temporal chirp of the laser pulse and the damage fluence of the MLD gratings. Each grating sees four beam reflections at four different heights. To fold the beam, a six-mirror assembly (effectively three periscopes) adjusts the beam height between grating passes and spatially inverts the chirped beam along the direction of propagation.

Autocorrelation measurements of the compressed IR pulse duration are shown in Fig. 7 (top left). The autocorrelation has a narrow (28 ps) central lobe and a wide pedestal; the latter contains approximately 70% of the total energy. The width of the central lobe is consistent with a 20 ps FWHM pulse duration. The measured pulse spectrum recorded with a $f = 1.5\tilde{\text{m}}$ McPherson spectrometer shows an amplified bandwidth of $0.25\tilde{\text{n}}\text{m}$ [Fig. 7 (top right)]. The oscillation in the spectrum with a 0.05 nm period is indicative of pre and post pulses spaced 75 ps apart. The poor temporal pusle compression we observed is caused by a periodic modulation in the CFBG dispersion, a problem being corrected in the next upgrade to the laser system.

Before delivery to the interaction point, the compressed IR beam can be frequency converted to attain appropriate energy ranges of the Compton generated γ-ray beam. The ILS can be reconfigured to provide either the fundamental or the 2nd or 3rd harmonic frequency. Frequency conversion is accomplished with large aperture DKDP crystals. Up to 170 mJ of 2ω light ($\lambda = 532\tilde{\text{n}}\text{m}$) is produced using a 30×30 mm aperture, 6 mm thick DKDP crystal cut for type II doubling. At 3ω, 120 mJ of 355 nm light is generated using two 60×60 mm aperture DKDP crystals. The doubling crystal is cut for Type I phasematching and the

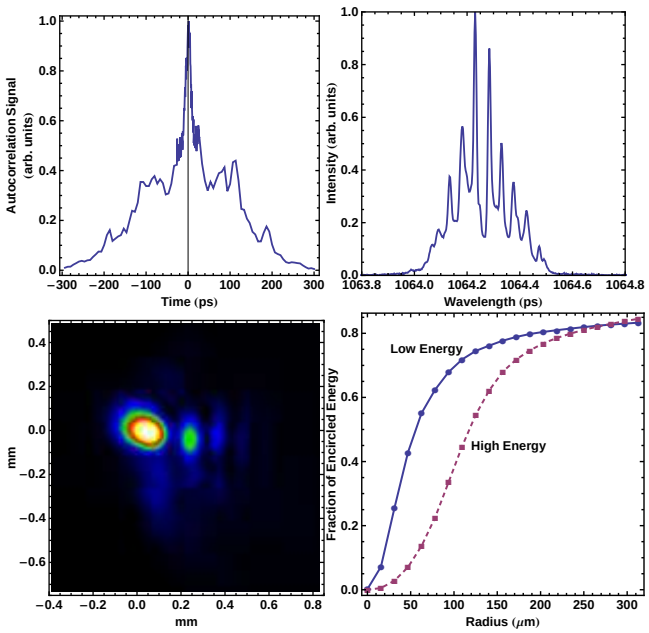

FIG. 7: Top left: autocorrelation trace of the compressed ILS IR pulse. Approximately 30% of the energy is in the central peak. Top right: spectrum of the compressed ILS IR pulse. Bottom left: profile of the ILS focal spot after an $f = 2.4$ m lens. Bottom right: fraction of total energy contained within an aperture of a given radius for low and high energy system output.

tripling crystal is cut for Type II phasematching, producing up to120 mJ of 3ω light. The typical energy jitter is 2% in the fundamental pulse, and 4% in the 2nd harmonic and 3rd harmonic.

The laser pulse is focused to the interaction point with an $f = 2.4$ m lens. Low order wavefront aberrations result in a focused beam that is twice the diffraction limit. Additionally, several up-stream optics, mainly laser rods and compressor mirrors, aperture the beam producing high frequency spatial modulation. At the beam focus, this results in a pedestal which contains a large fraction of the overall energy. The focal distribution of the 2ω light recorded with a 12-bit camera is shown in Fig. 7 (bottom left). Additional side lobes at the focus are indicative of beam clipping. In order to determine the generated γ-ray dose, an important figure of merit is the energy contained within the spot overlapped with the electron beam. Fig. 7 (bottom right) shows the encircled energy contained within an aperture of radius R. For a high energy (150 mJ) focused 532nm beam, 30% of the total energy is contained within a 100 μm radius aperture.

The time duration of the 2ω signal has not yet been measured quantitatively. Computer

simulations of the frequency doubling process, assuming a 1ω pulse which contains 30% of the total energy in the 20 ps central peak and the rest of the energy in a 600 ps wide pedestal, indicate that frequency conversion will slightly shorten the pulse length and suppress the pedestal due to the nonlinear nature of the process. After doubling, approximately 50% of the 2ω energy should be in the 16 ps central peak with the rest of the energy contained in the wide pedestal.

B. Electron Systems

Precision electron beam generation requires that the laser arrival time at the photocathode is synchronized to within 1° of phase to the accelerating rf in the photoinjector cavity; thus, the two systems must be locked to the same clock. As mentioned above, the laser is locked to a 40.7785 MHz reference crystal oscillator, the 70th subharmonic of the accelerator's 2.8545 GHz operating frequency. The laser photodiode signal, used to keep the laser locked to the master crystal and to generate the timing triggers for all the laser and accelerator systems, is also filtered to produce a sinusoidal rf signal that tracks the laser pulse train even if it drifts from the reference frequency. This signal is fed into a phase-locked coaxial resonant oscillator which puts out S-band rf phase-locked to the laser pulse train. The mW level rf power is distributed to a set of 6 modules consisting of a kW amplifier and pulsed klystron, producing 3-4 microsecond pulses of roughly 20 MW of peak rf power. These modules independently drive the photoinjector and the 5 separate accelerating sections, allowing independent phase and power control over each rf structure.

The T-REX injector is a 1.6 cell photo-cathode gun of the BNL/SLAC/UCLA/LLNL design [26]. There are, however, several key changes from previous designs [27]. Because on-axis laser injection is used, the 70° ports of the half cell were removed, making the half cell fully cylindrically symmetric. The full cell was also symmetrized to quadrupole moment by replacing the tuning plungers, which have been found to break down at high field and limit gun performance [28], with race-track shaped slots identical to the RF coupling slot.

Another significant change to the gun design was to increase the frequency separation of the 0- and π-modes. This modification was first implemented at SLAC in order to minimize the excitation of 0-mode fields which were found to have a detrimental effect on the beam emittance and energy spread [29]. The mode separation of the T-REX gun was increased to

12.3 MHz. PARMELA simulations were performed and indicate that the effect of the 0-mode is negligible at the larger mode separation, in agreement with the results of [29].

The photoinjector cathode is a 1 cm diameter, 2 μm thick layer of Mg sputter-coated onto the copper backplane of the half-cell cavity. When powered, the peak on-axis field in the gun reaches 120 MV/m. When illuminated with 17 μJ of light from the PDL, an 800 pC electron bunch is produced with a quantum efficiency (QE) of 1×10^{-4} at 30° injection phase. No efforts have been made at this point to improve the QE or the QE uniformity through *in situ* cleaning methods. At the entrance to the linac, the beam energy is 5.5 MeV with a normalized emittance of 1.8 mm mrad measured with a pepper-pot mask. A detailed study of the beam dynamics of this low energy beamline is forthcoming [30].

The beam generated by the photoinjector is then coupled into LLNL's linear accelerator [31]. Originally designed for high current beams used for neutron production, some upgrades to the system were required. An additional 8 ft. SLAC-type S-band disk-loaded traveling-wave linac section was added to the preexisting architecture to allow us to reach an endpoint energy of 120 MeV, bringing the total number of identical accelerating sections up to 5. The beam focussing solenoids on each section were not used due to concerns about the alignment of the magnetic and rf axis and the potential for emittance growth from quadrupole field errors in the presence of a solenoidal field [32]. Instead, quadrupole doublets or triplets were inserted between the sections to control the beam growth.

The emittance of the electron beam was measured at the end of the accelerator using a quadrupole scan, and yielded a normalized rms emittance of $\epsilon_{n,x} = 4, \epsilon_{n,y} = 8$ mm mrad. Based on the beam energy, charge, and drift length in the system, space-charge forces had a negligible effect on this measurement [33]. The most likely source of the emittance growth is the asymmetric waveguide feed on the accelerator sections, a well known issue for the SLAC section design [32, 34].

C. Interaction Region

The interaction architecture was driven by the requirement of having a 180° interaction geometry to maximize the overlap between the laser and electron bunch (thereby maximizing γ-ray flux) and the desired spot size for the interaction. The interaction spot size was chosen based on a study of the spectrum of γ-rays generated by different electron focus sizes.

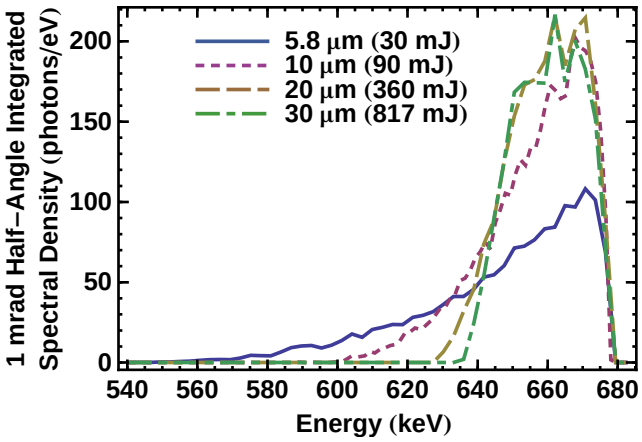

FIG. 8: Plot of the predicted integrated spectrum of the γ-ray source as a function of electron rms spot size. Smaller sizes show broadening due to the large angular distribution of the electron beam.

PARMELA [35] simulations of the full accelerator system, including a quadrupole triplet to focus the final beam, and assuming the optimal gun parameters as discussed in [24], were run to produce electron distributions of different focal sizes. These distributions were then fed into the scattering code [36] to calculate the γ-ray spectra over a 1 mrad half-angle cone (the expected size of the largest aperture we'd use to collimate the beam), and the results are shown in Fig. 8. The laser spot size was chosen to match the electron spot size, and the laser energy set to keep $a_0^2 = 0.1\%$ to avoid spectrum-broadening nonlinearities in the scattering (which the code doesn't include). For small spot sizes, a significant broadening of the spectrum is seen, a result of the large angular distribution applied to the electrons to get the bunch to focus tightly. Once an rms size of $\sigma_{x,y} = 20$ μm is reached, however, the bandwidth is limited mostly by the inherent single-electron bandwidth of the included solid angle, which for $\gamma = 220$ is 4.6%. Any spots larger than 20 μm require significantly more laser energy to keep the photon density the same, but don't provide any increase in the number of photons per eV that are generated. In fact, since the spot size is increasing, the overall brightness of the source goes down. Therefore a $\sigma_{x,y} = 20$ μm spot was chosen as the design point.

This spot size requirement implies for the laser that $f/\# = \frac{\pi w_0}{2\lambda} = \frac{\pi \sigma_x}{\lambda} \geq 60$ for $\lambda \leq 1.064$ μm is needed for the beam, which allows for a long focal length. Thus the interaction geometry shown in Fig. 9 is the simplest choice. The electron beam is brought to a focus

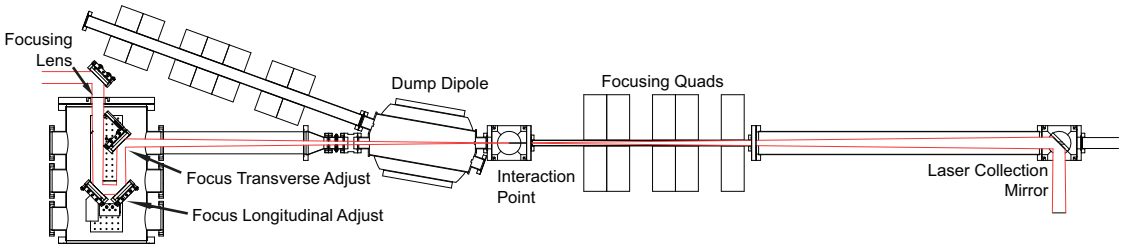

FIG. 9: Layout of the T-REX interaction region.

by a pair of quadrupole triplets. The first triplet is designed to match the spot size and emittance at the end of the acceleration sections to that needed to produce the proper focus. Then a high-gradient (up to 15 T/m) quadrupole triplet brings the spot size down to the desired spot size. This system is designed to get beams with a normalized emittance up to 5 mm mrad to a 20 μm focus 25 cm past the end of the last magnet. After the interaction, the electron beam is bent off the main axis by a 20° dipole magnet which also serves as an electron energy diagnostic. A third quadrupole triplet then captures the expanded electron beam and transports it to a well-shielded beam dump.

Meanwhile, the laser is focused by a $f = 2.4$ m lens which also serves as the window into the linac vacuum system. A pair of mirrors on a translation stage allow the position of the focus to be moved longitudinally about the interaction point, and a final motorized turning mirror allows the transverse positioning of the laser focus. Coupling that with a translation stage before the focusing lens to allow tweaking of the time of arrival of the laser, the system has 4D adjustment to get the laser to hit the electron beam at the interaction point.

Another focal length f past the interaction point, a dichroic mirror with a 1 cm hole in the center (to pass the electron beam) can be used to collect the residual laser light. Placing a matching mirror with a hole $2f$ before the focusing lens will cause that upstream hole to be imaged onto the dump mirror, preventing any light from propagating up the accelerator structure. The back of this mirror can be silvered to allow optical transitition radiation (OTR) imaging of the electron beam position on the back side to facilitate alignment of the beam through the optic's aperture. Simulations of the modified laser profile focusing and scattering from the electron beam show that the hole in the center of the laser before focusing doesn't affect electron production at the interaction point. With this scheme, the laser energy can be collected either for diagnostics or for recirculation of the unused photons [37]. Although demonstrated in the 3ω runs, the optic was removed when the system was

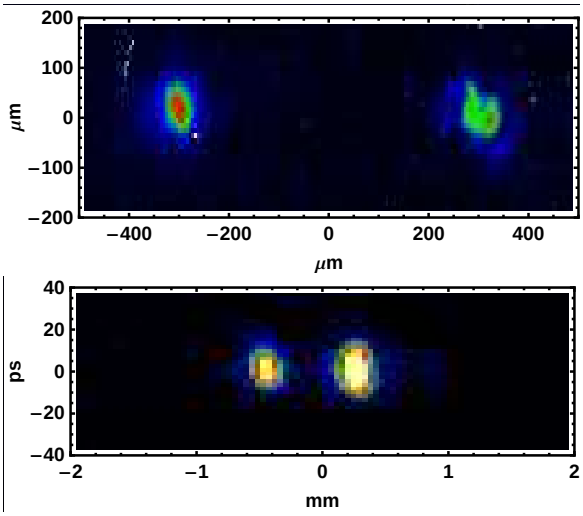

FIG. 10: Images of the laser and electron beams at the interaction point. Top: Beam spatial profile on alignment cube (electrons left, laser right). Bottom: Streak camera image of the two beams on the alignment cube (laser left, electrons right)

switched to 1ω operation and not reinstalled for further experiments, since the collected beam wasn't being used.

To establish the relative alignment of the laser and electron beams, an optically polished 8 mm nickel cube, attached to a two-axis translation stage, is located at the interaction point [38]. Oriented with the vertical faces at 45° to the electron-laser beamline, the laser (significantly attenuated in energy) will reflect off the surface and the electron beam will generate OTR light at an angle corresponding to the reflection angle. This light is imaged with a camera to ensure the beams are aligned vertically, and the overlap horizontally can be determined by seeing the beams meet at the edge [Fig. 10 (top)]. The light is also imaged onto a Imacon 500 Series streak camera (maximum resolution 2 ps) to allow the adjustment of the laser delay to get the correct temporal overlap [Fig. 10 (bottom)]. The timing of the interaction laser pulse is adjusted coarsely (in 24 ns steps) by selecting the appropriate pulse from the 40.7785 MHz oscillator with the fiber AOMs and the ILS pulse slicer to amplify, on a finer scale (to within ~ 1 ns) by adding in an appropriate length of fiber to the transport line from the front end of the system, and finally to within 10 ps by adjusting the position of the retroreflecting mirror in the middle of the 6 mm rod assembly in the amplifier chain of the ILS.

Measurement of the two beams on the alignment cube shown in Fig. 10 yield a gaussian

fit with an rms spot size of 34 × 38 μm for the laser focus and 23 × 42 μm for the electron focus. The streak camera images provide evidence that the pulses are on the order of 10 ps in length. Analysis of several consecutive electron beam images at the cube provides a measurement of the beam centering jitter, which is on the order of 20 μm rms. Performing a similar analysis on an image of the beam after the dipole magnet allows an estimate of the pointing jitter of the beam. We observe an angular jitter of 1.2 mrad in the x direction (the direction of the dipole deflection) and 0.6 mrad in the y direction. In the x direction the angular jitter is a combination of both beam pointing jitter and shot-to-shot energy jitter. Based on jitter measurements before the final-focussing quadrupoles and a matrix analysis of the focal region transport, the energy jitter is a minimal contribution to the observed jitter. This angular jitter is significant for the γ-ray production because of the dependance of the scattered photon energy on the observation angle. Integrating over numerous shots, a large pointing jitter behaves identically to a large emittance in terms of the generated photon bandwidth. The position jitter has a direct impact on the total scattered γ-ray flux, and is thus essential to minimize.

D. γ-Ray Diagnostics

1. Spatial and temporal measurements

The γ-rays are detected on axis by a system which is composed of a 16 bit Intensified Charge Coupled Device (ICCD) Andor camera and a 3:1 optical fiber reducer coupled to the camera. The ICCD chip is an array of 1024×1024 13 μm size pixels coupled to a 1:1 optical fiber bundle, which, with the reducer demagnification, provides a 4×4 cm^2 detection surface. The fiber reducer is coupled to a 140 μm Cesium Iodine scintillator doped with Thallium [CsI(Tl)], which isotropically converts the γ-rays into visible green light at a rate of 54 photons/keV. The scintillator is protected with a 0.5 mm thick Beryllium (Be) window to block any laser light remaining and to cut detected noise from low energy x-rays scattering in the accelerator cave. The system was calibrated by using a ^{137}Cs radioisotope source delivering 2.85×10^5 photons/s at 662 keV. The measurements indicate 70 counts/photon at this energy. From that point, the number of counts per γ-ray photon produced by the detection system can be extrapolated by using the γ-ray absorption curve in CsI(Tl), which

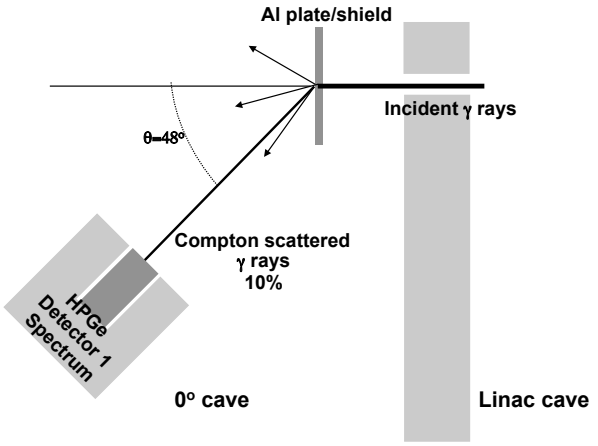

FIG. 11: Layout of the detection system. The γ-rays are detected by a HPGe detector after being Compton scattered off an Al plate at 48 degrees

can be found in the NIST X-COM database [39]:

$$C(E) = \frac{E}{E_0} C(E_0) \frac{1 - e^{-\rho\mu(E)\Delta}}{1 - e^{-\rho\mu(E_0)\Delta}}, \tag{17}$$

where $\Delta = 140$ μm is the scintillator thickness, E_0=662 keV is the energy of the calibration source, r=4.51 g/cm^3 is the density of CsI(Tl), and $\mu(E)$ is the mass absorption coefficient, in square centimeters per gram.

2. Spectral measurements

Several techniques are currently available to measure x-ray spectra, including Bragg diffraction crystals, filters relying on x-ray attenuation in materials, and photon-counting methods with scintillators or x-ray diodes. As the lattice spacing for a diffraction crystal has to be on the order of the wavelength of the diffracted radiation to obtain a good resolution and efficiency, no crystal allows us to use this technique at energies of a few 100 keV and above. Using filters in our case is impractical because high Z and very thick materials would be needed, and the resolution of the measurement would be poor. For our spectral experiments we decided to use a detector operating in a statistical single photon counting mode.

In the present geometry, the γ-ray detector would have to be directly in the high energy Bremsstrahlung produced by the dark current of the linac if we want to measure the spectrum

on-axis. This yields background levels that are incompatible with single photon counting. To avoid this problem, we chose a geometry where the γ-rays are detected by a High Purity Germanium detector (HPGe) at an angle θ=48° with respect to the main beam axis, after being scattered off a 1/8 inch thick Aluminum (Al) plate located 20 meters away from the interaction point, in a room where the system is shielded by concrete walls. With this layout, as depicted on Figure 11, the scattered γ-rays of energy E_γ are related to the incident γ-rays of energy E_γ by the Compton scattering relation:

$$E_\gamma^{'} = \frac{E_\gamma}{1 + \frac{E_\gamma}{E_0}(1 - \cos\theta)}, \tag{18}$$

where E_0=0.511 MeV is the electron rest energy.

This method has two advantages: the detector is placed far from the on-axis Bremsstrahlung background and the Al plate preferentially scatters the lower energy X-rays. For example, 7% of 500 keV radiation is attenuated by the plate while only 2.5% of 5 MeV γ-rays are. The thickness of the Al plate was adjusted so that a count rate of 0.2 photon/shot was observed on the HPGe, which we judged as the best trade off between pile up and efficiency. The detector is made of a high purity germanium crystal which is 8 cm long and 6 cm in diameter. The resolution, measured with a ^{137}Cs radioisotope source was found to be 2.8 keV at 662 keV (0.4%). The detector head is placed 150 cm away from the Al plate, which corresponds to a angle of 2.3° subtended by the crystal. With a scattering angle of 48 degrees and a central energy of 478 keV (scattered energy 365 keV) this means an uncertainty of 13 keV on the spectrum measurement (relative uncertainty of 3.5 %). The resolution of our spectrum is thus limited by the geometry of our detection system. The output signal of the detector, biased at +4000 Volts, is shaped to a pulse with an amplitude ranging from 1 to 10 Volts and with a Full Width Half Maximum (FWHM) of several μs. This pulse is then sent to a 8192-channel Analog to Digital Converter (ADC) which retrieves the spectrum. The ADC was synchronized to the rf power of the linac with a 8 μs gate, to ensure that only photon events related to the linac and Compton scattered γ-rays at 10 Hz where recorded. This was necessary because of the natural activation present in the room, at a rate of several kHz, which makes the detection of the Compton scattered γ-rays spectrum impossible. The settings of the shaper and ADC allowed us to measure spectra in the 10 keV-1.6 MeV range with a dispersion of 0.2 keV/channel.

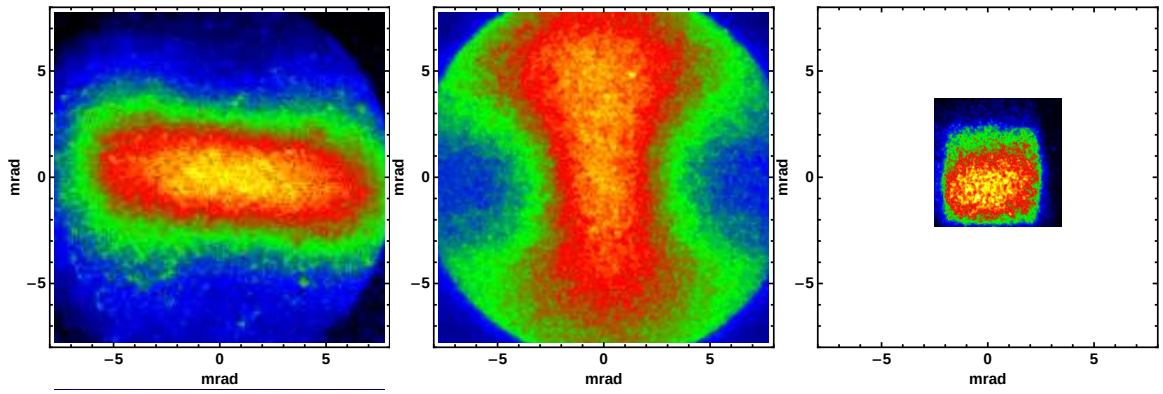

FIG. 12: γ-ray beam profiles from scintillator-coupled CCD cameras for the three laser frequencies. The beam energies are: left - 295 keV (128.4 MeV + 1ω), center - 465 keV (114 MeV + 2ω), right - 909 keV (130 MeV + 3ω)

III. SOURCE CHARACTERIZATION

A. Initial γ-rays

γ-rays were initially generated in 3 different laser configurations: 1ω where the ILS pulse was used without any frequency conversion ($\lambda_{1\omega} = 1064$ nm and $E_{x,1\omega} \approx 225$ keV), 2ω where the laser is frequency doubled ($\lambda_{2\omega} = 532$ nm and $E_{x,2\omega} \approx 450$ keV), and 3ω where the laser is frequency tripled ($\lambda_{3\omega} = 355$ nm and $E_{x,3\omega} \approx 675$ keV - all assuming $\gamma \approx 220$ for the electron beam, a typical number). Two different charge coupled device (CCD) cameras were used to detect the produced γ-rays. The first, used for the 1ω scattering, was a Princeton Instruments 16-bit, 1340×1300-pixel, 2.54 mm × 2.54 mm CCD coupled via a 3:1 demagnifying fiber optic bundle to a 145-μm thick CsI(Tl) scintillator. The second, used for the 2ω and 3ω measurements, was the Andor iStar camera described in Section II D. For the 3ω scattering, this system was fiber-optically coupled to a 150 μm CsI(Tl) scintillator with no demagnification of the beam (thus only showing a portion of the profile). For the 2ω runs, a fiber taper with a 3:1 demagnification coupled the camera to the scintillator, giving a 4 cm × 4 cm observation area.

Figure 12 shows the images from the cameras for the three energies. The 1ω (left) and 2ω (center) images show a hard round aperture which is the steel flange holding the 300 μm Be plate used as a vacuum window. The 3ω image (right) shows a 1 cm square aperture in a lead brick. This aperture was used to give a discernable profile to the beam because the

beam overfilled the camera's observation window. The distored shape is a result of the $\sin^2$ distribution of the dipole scattering in the electron rest frame. In the electron rest frame, the null points of the radition pattern are at 90° to the beamline axis, along the direction of the laser polarization. However, the Lorentz transformation of angles when moving to the lab frame gives

$$\cos\theta = \frac{\cos\theta' + \beta}{1 + \beta\cos\theta'} \tag{19}$$

so when $\theta' = 90°$ and $\beta = \sqrt{1 - \frac{1}{\gamma^2}}$ with $\gamma = 220$, we find $\theta = 4.5$ mrad. In the 1ω case, the laser is polarized vertically, leaving the nulls of the radiation pattern aligned vertically as well. As a result of the frequency doubling process, the laser is polarized horizontally in the 2ω case with a consequent horizontal alignment of the nulls.

B. Source Characterization at 2ω

On axis, if we have 116 MeV electrons and 532 nm laser light, the scattered energy is 478 keV, according to (1). Our motivation for selecting this energy was to detect nuclear resonance fluorescence (NRF) in ^{7}Li, which has a strong line at 478 keV. At this energy, the following features of the source have been studied: γ-ray beam profile and dose, source size, dose as a function of delay between the laser and the electron beam, on and off-axis spectrum, and tunability with the electron beam energy.

1. Beam profile and dose

The spatial beam profile was measured with the Andor camera using 15 s integration time (150 shots) to obtain good statistics. Fig. 13 shows a typical γ-ray image recorded with those conditions 2 m away from the interaction region. The divergence is lower along the horizontal direction due to polarization effects [40]. The full width half maximum (FWHM) of the beam is 6.0 mrad and 10.4 mrad along the horizontal (x) and vertical (y) axis respectively. By integrating the total counts from the beam profile in Fig. 13, one obtains a total number of 1.6×10^5 photons/shot.

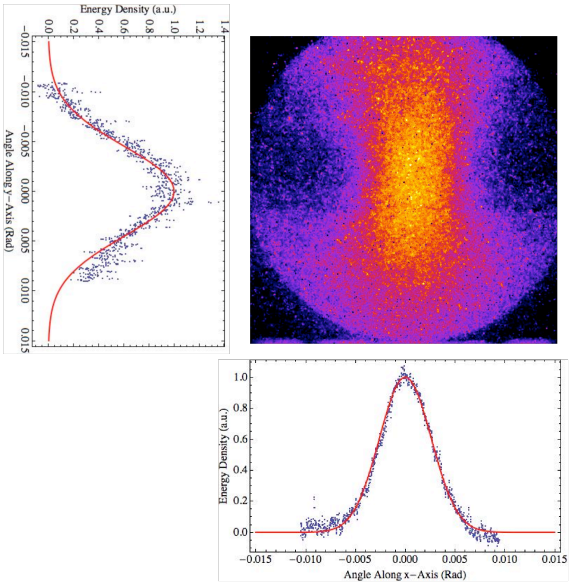

FIG. 13: False color image of the γ-rays recorded by the ICCD over 15 s of integration and 2 m away from the interaction region. On the bottom and left of the image the angular energy distribution are displayed for the horizontal (x) and vertical (y) axis respectively. The solid curves represent the Gaussian fit of the experimental data points (dots).

2. X-ray intensity as a function of delay between laser and electron beams

When the laser and electron beams are collinear, varying the delay is equivalent to a change in the laser spot size from its minimum waist w_0 and photon density at the interaction point. Thus, the x-ray intensity as a function of the delay between the two beams varies as a Lorentzian $1/[1+(z/z_0)^2]$, where $z_0 = \pi w_0^2/\lambda_0$ is the Rayleigh length. Since the beta function of the electron beam focusing line is longer than the Rayleigh length in our geometry, the x-ray intensity variation is dominated by the change in the laser spot size. We have used an optical delay line to vary the timing between the laser pulse and the electron bunch, which allowed us to measure the x-ray intensity change, averaged over 25 shots, displayed on Fig. 14. The experimental curve can be fitted by a Lorentzian of width $\Delta t = 25$ ps, which corresponds to a Rayleigh length $z_0 = c\Delta t = 7.5$ mm. The focal spot inferred from

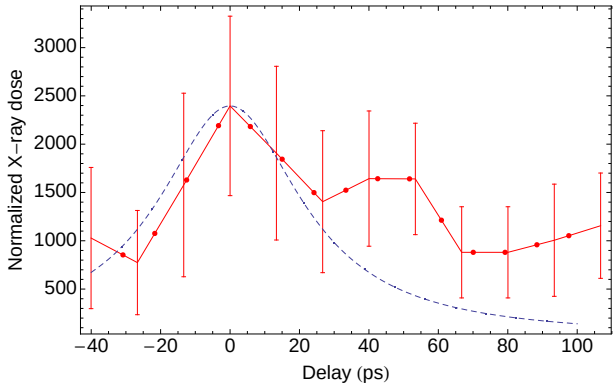

FIG. 14: Experimentally measured variation of the x-ray intensity as a function of the delay t between the laser and the x-ray beams (dots) and Lorentzian fit $1/[1+(t/\Delta t)^2]$ where $\Delta t = 25$ ps (dashed curve). The error bars are the standard deviation of the intensity averaged over 25 shots.

this measurement is 29 μm at $\lambda_0 = 532$ nm. This value is 2.5 times smaller than the actual focal spot size (w_0 =75 μm), indicating a non-diffraction limited laser operation.

3. On axis spectra

In Fig. 15, the spectrum of on-axis photons is shown. To faithfully measure the on-axis spectrum, we have used a 6 mm lead collimator to aperture the beam. The collimator was aligned to the center of the spatial image, as shown in the inset of Fig. 15. The spectrum displayed in Fig. 15 corresponds to 5 keV bins and to 6 hours of data recorded at 10 Hz. The measured spectrum is compared with the simulated pulse height spectrum expected for single-photon counting.

As can be seen in Fig. 15, the spectrum has several distinctive features. The tail after 400 keV is mainly due to the high energy Bremsstrahlung and to pile-up (multiple-photon events) in the detector. The main peak has a maximum for 365 keV, which corresponds to an incident energy of 478 keV. The FWHM of this peak is 55 keV (within limitation of 5 keV bins), which corresponds to a relative bandwidth of 15%. By differentiating (18), it corresponds to an initial source bandwidth of 12 %.

At energies lower than 250 keV a broad continuum can be seen, on which two other peaks (respectively located around 80 keV and 110 keV) are superposed. Those are not physical features of the source itself but are the result of several interaction processes, which

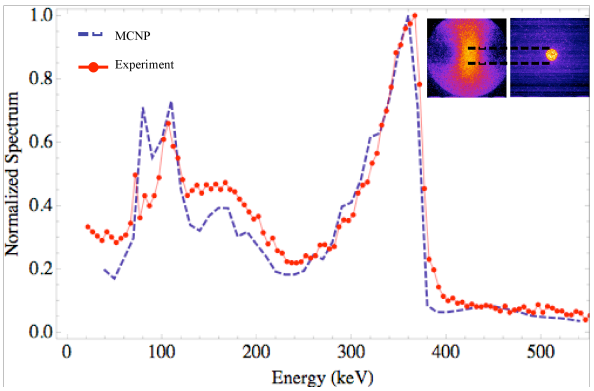

FIG. 15: On axis spectrum recorded after scattering off the Al plate and corresponding Monte Carlo simulation. The images correspond to the full beam and the signal transmitted through the collimator respectively

can be very well tracked and reproduced by Monte-Carlo simulations. For modeling we used the MCNP5 code [41], with modifications to include Compton scattering of linearly polarized photons [42]. The γ-ray source spectrum was calculated using the Mathematica script described in section II, and used by MCNP5 to sample the energy of each source photon in the incident pencil beam (5 cm diameter). The polarization was assumed to be 100% in the horizontal plane (including the beam axis and HPGe detector). All the major components of the experimental setup, such as walls, air and lead shielding were implemented in the MCNP5 geometry description. Figure 15 shows the simulated pulse height spectrum expected for single-photon counting.

The continuum below 250 keV is due to incomplete energy absorption (elastic Compton scattering) in the detector itself. The broad peak at 110 keV arises from double Compton scattering off the Al plate and adjacent wall, followed by photoabsorption in the Ge Detector. Since the detector is shielded with lead, the first peak is due to X-rays coming from the lead K_α and K_β lines, respectively at 72.8 keV, 75 keV, 84.9 keV and 87.3 keV. The 5 keV binning applied to the spectrum does not allow us to distinguish those lines.

4. Off-axis X-ray spectra: energy-angle correlation

The energies of γ-rays produced by Compton scattering vary within the cone of radiation. According to (1), the highest γ-ray energy $4\gamma^2 E_L$ is on axis and the off axis γ-ray energies

should be lower. To verify this characteristic property of Compton scattering we have measured the spectrum off-axis, at two different positions, for an electron beam energy of 125 MeV and a laser wavelength of 532 nm. To do so, we have used the same 6 mm lead aperture as for the on-axis measurement, and to alter the direction of the γ-ray beam, the incident electron beam was deflected with two small steering magnets, so that the position of the electrons at the interaction point was fixed, while the beam angle could be varied by several milliradians. It was not possible to move the collimator instead as it is precisely pointing toward the shielded room where the detectors are. Our measurements correspond to a 3 mrad off-axis measurement in the upper part of the beam and to a 2.5 mrad off-axis measurement in the lower part of the beam, as shown in Fig. 16. As expected, for both lobes the spectrum is broader than on-axis, with a peak at $\sim$250 keV for the upper-lobe and a peak at $\sim$290 keV for the lower lobe as seen on the plots resulting from the Monte-Carlo simulation with MCNP5. The parameters of the simulation are the same as for the on-axis spectrum calculation except for the angle of observation that has been changed according to the upper and lower part of the beam.

5. Energy scaling with the electron beam energy

On-axis, the Compton scattered γ-ray energy theoretically scales with $4\gamma^2$ for a given laser energy (if we neglect the recoil), which we verified by tuning the electron beam to four different energies: 116 MeV, 101 MeV, 85 MeV and 68 MeV, and by measuring the spectrum for each case. Identical alignment of the collimator with the center of the beam has been maintained throughout the measurement. The four spectra are displayed in the top part of Fig. 17, where each data set corresponds to 1h of acquisition at 10 Hz and in a single photon counting mode (rate of 20%). The 116 MeV data correspond to 6.5 hours of acquisition and has been normalized to be within the same amplitude as the other plots. From this measurement, the incident peak γ-ray energy on the Al plate can be retrieved by using (18). The bottom part of Fig. 17 displays the incident peak γ-ray energy (inferred from the experimental data) versus the electron relativistic factor γ. On top of the data points is plotted the theoretical expected γ-ray energy $4\gamma^2 E_L$, where $E_L = 2.33$ eV is the laser energy. This shows good agreement and validates the $4\gamma^2$ signature scaling law of laser-based Compton scattering for our source.

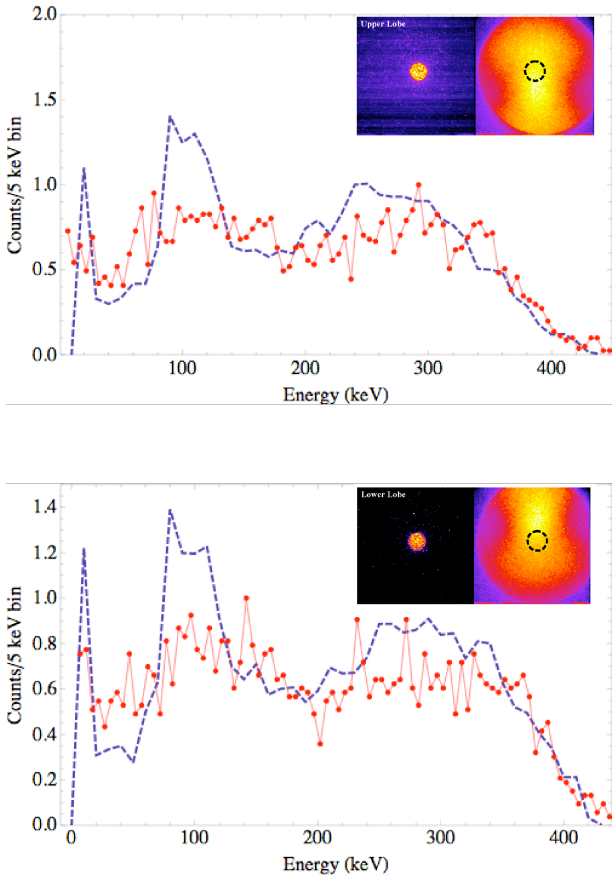

FIG. 16: Off-axis spectra measured (dots) for the upper lobe (3 mrad away from the center) and the lower lobe (2.5 mrad away from the center), with the corresponding Monte Carlo simulations (dashed curves)

6. High energy Bremsstrahlung

The linac itself is a source of high energy γ-rays because it is well known that the electromagnetic field in a high gradient RF structure can cause electron emission from the copper walls of the accelerating sections. Those electrons can then be accelerated by the fields and interact with metal present in the linac, which potentially yields high energy γ-rays on axis. The dark current can reduce the signal to noise ratio for the Compton scattered γ-rays. To measure this background, we placed one HPGe directly in the incident beam. During this measurement, only the RF power of the linac was enabled while all the lasers (ILS and PDL) where turned off. In addition, to avoid saturation on the detector, we placed 5 inches of lead in the beam path to reduce the count rate to 0.2/pulse. Since low energy x-rays

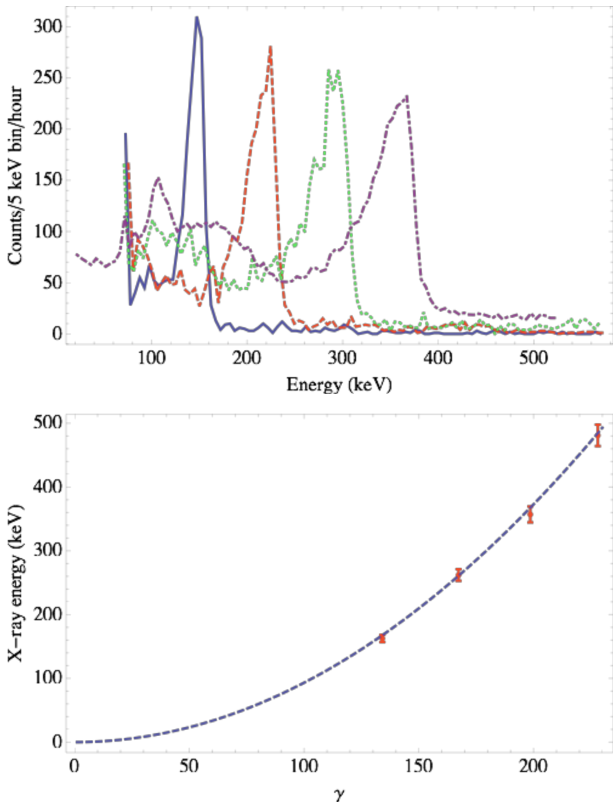

FIG. 17: Top: experimentally measured on-axis spectra for electron beam energies of 68 MeV (solid), 85 MeV (dashed), 101 MeV (dotted) and 116 MeV (dot-dashed). Bottom: experimentally measured peak γ-ray energy points versus γ and theoretical peak γ-ray energy $E_x = 4\gamma^2 E_L$

are highly attenuated by the lead absorber, only Bremsstrahlung arising from the dark current was measured. The resulting spectrum is presented in Fig. 18, with a inset showing the spectral region near 0.5 MeV, on which the 0.511 MeV line from electron-positron annihilation pairs can well be seen. The incident number of γ-ray photons on the detector can be simply retrieved by taking into account the attenuation through 5 inches of lead (NIST-XCom database) and the efficiency of the detector (50%). At 1 MeV, one finds 1.1 photons/0.1%BW/shot from Bremsstrahlung.

C. Summary: On-Axis Brightness

With the experimental results obtained throughout the experiments, one can compute the on-axis brightness of the source. The only parameter that has not been directly mea-

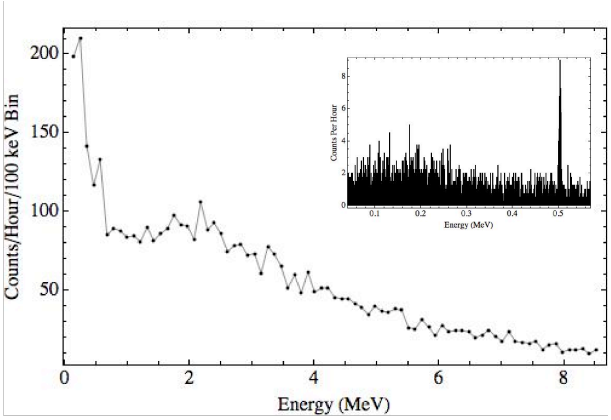

FIG. 18: High energy bremsstrahlung arising from the linac dark current measured between 0 and 8 MeV (100 keV bins) and behind 5 inches of lead. The inset represents the raw data (0.2 keV/channel) in the neighborhood of 0.5 MeV

sured during this experimental campaign is the source size. However, it can be inferred from the overlap of the electron beam and laser beam focal spots, which have been measured at 40 μm (rms) and 75 μm (FWHM) respectively. With a spectral bandwidth of 12% at 478 keV, a pulse duration of 10 ps (inferred from the laser and electron beam durations), a dose of 1.6×10^5 photons/shot and a divergence of $10.4{\times}6$ mrad^2, one obtains an on axis peak brightness of $1.5{\times}10^{15}$ photons/mm^2/mrad^2/s/0.1%bandwidth, which is roughly the brightness of the APS synchrotron at this energy, currently the brightest synchrotron in the United States. However, since the main goal of this experiment was the proof of principle demonstration of NRF, neither the laser nor the electron beam where fully optimized. However, by using the code described in this paper and that has been benchmarked against our experimental results, we can predict a peak brightness on the order of $1{\times}10^{21}$ photons/mm^2/mrad^2/s/0.1%bandwidth at 478 keV by using state of the art parameters for the electron and laser beams, as shown in Fig 19.

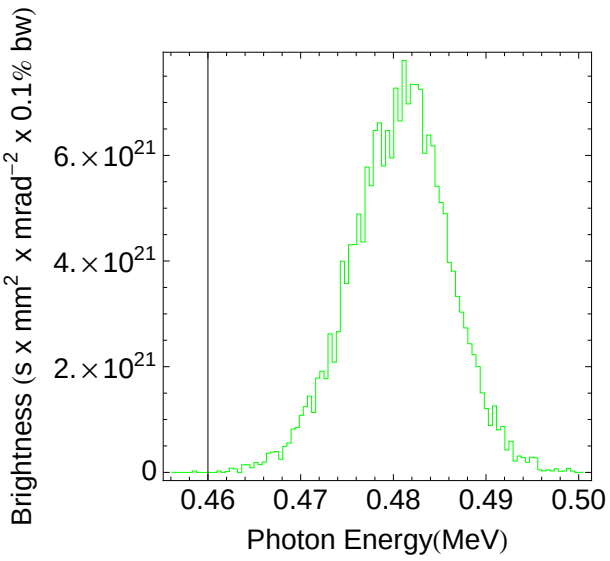

FIG. 19: On axis spectrum calculated with a 1 nC, 1 mm mrad emittance and 20 μm electron beam spot size (rms) and a 1J, 20 μm FWHM size laser spot and no jitter.

IV. DETECTION OF NUCLEAR RESONANCE FLUORESCENCE IN ^{7}Li

A. NRF detection setup

In addition to measuring the properties of the source, we have used it to detect the NRF line of ^{7}Li at 478 keV. For this, we used a 8-cm diameter plastic bottle containing 225 g of LiH with a density of 0.36 g/cm^3. The sample was located in the shielded 0° cave, about 20 meters away from the source which is still collimated by the 6-mm lead aperture. When the beam interacts with the lithium, its diameter is on the order of 4 cm. The NRF scattered photons from the ^{7}Li are detected by a second HPGe, similar in size, resolution and efficiency to the one used for the spectral measurements. As depicted in Fig. 20, the detector is placed at 90° with respect to the incident beam axis, 15 cm away from the center of the beam. As only 7% of the incident γ-rays are attenuated by the Al plate, we have kept the spectral diagnostic in order to verify the proper tuning of the beam throughout the measurement. With the γ-ray production described above at 478 keV, NRF photons were expected to be scattered isotropically at a rate of 16 photons/hour. The HPGe detector was positioned in the X-ray polarization plane to maximize the NRF signal from the M1 transition in ^{7}Li [43]. A scattering angle of 90° was chosen in order to minimize the amount of Compton

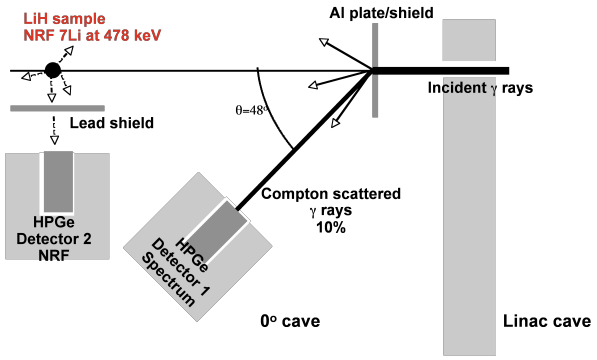

FIG. 20: NRF detection setup

scatter background from the LiH target [44]. A 1 cm thick Pb absorber in front of the HPGe detector reduced the count rate to 10%. It also serves as a demonstration that detecting low-Z and low-density material behind high-Z, high-density material is feasible with this process.

B. NRF Results

NRF data have been acquired for 7.5 hours at a 10 Hz repetition rate and the full spectrum obtained on the detector between 0 and 1.6 MeV is displayed in Fig. 21 on a logarithmic scale. Besides the 478 keV NRF line from ^{7}Li, several distinguishable features can be observed on this plot. The continuum centered around 250 keV corresponds to Compton Scattering of the 478 keV radiation off the LiH sample at an angle of 90°. As in the source spectrum, the peaks corresponding to the lead fluorescence around 80 keV are present. The line at 511 keV results from the $e^{+} - e^{-}$ annihilation pairs created by the high energy Bremsstrahlung from the linac (this line remains present when we block the ILS). The lines at 1.17 MeV and 1.33 arise from ^{60}Co activation naturally present in the cave walls.

A closer look at the scattered spectrum between 460 keV and 540 keV, showing the NRF line and the 511 keV line, indicates a detection confidence level of 6σ.

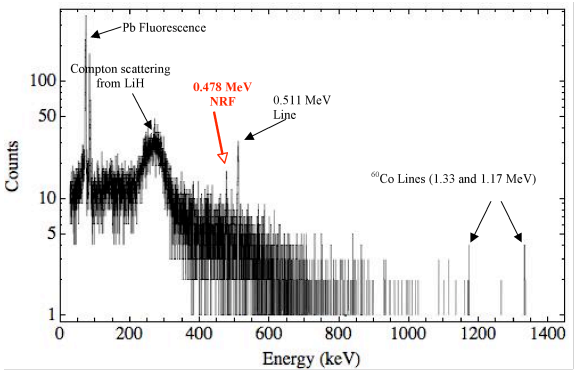

FIG. 21: NRF spectrum and features

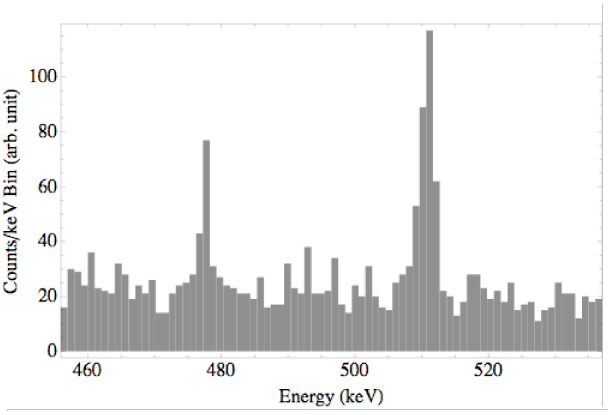

FIG. 22: NRF scattered spectrum between 460 keV and 540 keV, showing the NRF line with a 6σ confidence level and the 511 keV line

C. Notch detection

Having detected NRF from ^{7}Li, we investigated another method to ascertain the presence or absence of a given isotope that has the potential to yield lower false positive and negative rates [11]. In this method, first proposed by Bertozzi [45], γ-rays are transmitted through the material under interrogation to a reference sample containing the isotope of interest. If NRF is detected from the reference, one can conclude that the interrogated material did not contain the isotope. If no NRF is observed, either the resonant photons have been scattered by the isotope in the interrogated sample, or the material is optically too thick; the latter case can be ruled out by a simple transmission measurement. Since this method relies on the creation of a notch in the transmitted spectrum at the NRF energy by the isotope of

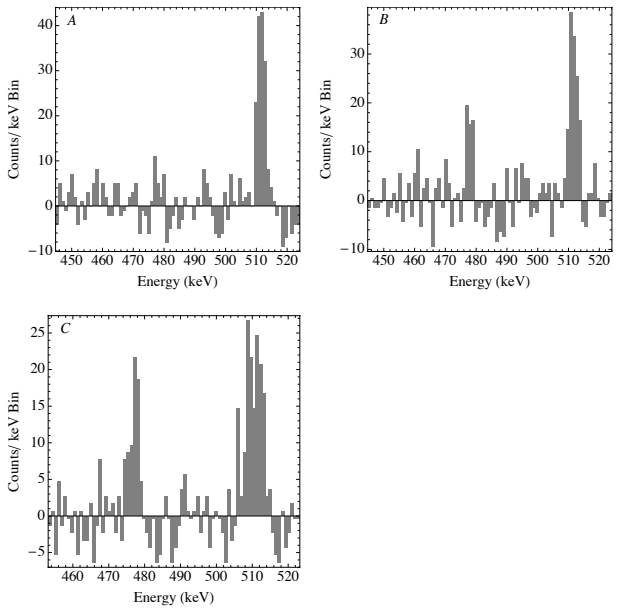

FIG. 23: NRF detection in ^{7}Li with two samples: output of reference detector when the LiH is out of the beam (A) and in (B), and output of test detector when the LiH is in the beam (C).

interest, the advantages of narrow-band, highly collimated light sources are clear.

We placed an identical test LiH sample in the beam path before the reference LiH bottle already present. It was mounted on a horizontal translation stage so that we could observe the effect on the NRF scattered spectrum in the reference sample. With the test sample, we also placed another HPGe, in the same configuration as for the reference LiH sample. The data displayed in Fig. 23 represent the scattered spectra obtained on both detectors when the LiH is in and out of the beam, with background subtraction. In each spectrum the 511 keV line can be observed, as in Fig. 21. The bottom image is the data from the test detector, which faces the removable LiH bottle. When the test sample is in the beam, the NRF line is observed on the test detector and not on the reference one. When the LiH sample is pulled out, the NRF line appears on the reference detector. The lines appear wider on the bottom image because the test HPGe detector used has a larger resolution (4 keV vs. 2.8 keV).

V. CONCLUSIONS

We have commissioned a tunable Compton-scattering-based γ-ray source and generated energies ranging from 75 to 900 keV. This source has been exhaustively studied by a series of different diagnostics, allowing us to measure spectral (12% bandwidth at 478 keV) and spatial data (low divenrgence), as well as characteristic signatures of the Compton scattering mechanism ($4\gamma^2$ scaling and energy-angle correlation). The key parameter of this source is it's high brightness, 1.5×10^{15} photons/mm^2/mrad^2/s/0.1%bandwidth at MeV-range energies. We have demonstrated, by detecting nuclear resonance fluorescence from ^{7}Li at 478 keV, that this new class of Compton scattering sources will have tremendous applications in nuclear photo-science.

Having successfully demonstrated much of the system architecture, work has begun on designing a system reaching more penetrating γ-ray energies in the 2 MeV range. A new linac structure will be needed to generate the electron beam energy needed and to correct some of the known errors in the stability of the rf power and the symmetry of the accelerating fields. Also, the new accelerator design will include provisions to move the electron beam off the main accelerating axis to minimize on-axis dark current backgrounds, which have been seen to be an issue. The pulse shaping in the PDL laser will be refined to produce a more uniform pulse, and increasing the fiber lasers energy to the level where a regenerative amplifier is not needed would help both the shot-to-shot energy stability as well as allow for compression to a shorter pulse, hopefully improving the emittance of the electron beam. Finally, the ILS is being redesigned to minimize the aberrations that led to the poor focal spot of the beam and dispersion ripple that caused the large pedestal observed in the autocorrelations. All these improvements should allow for a significant improvement in both the observed γ-ray flux and brightness.

Acknowledgments

The photoinjector was designed in collaboration with H. Badakov, P. Frigola, A. Fukusawa, B. O'Shea and J. Rosenzweig of UCLA. We would like to thank John Heebner, Chris Ebbers, Andy Bayramian, and Scott Fochs for their help in the rapid assembly of the regenerative amplifier and ILS, Jay Dawson for his help in diagnosing PDL recompression

efforts, and Igor Jovanovic for his work on the initial stages of the laser design. This work performed under the auspices of the U.S. Department of Energy by Lawrence Livermore National Laboratory under Contract DE-AC52-07NA27344. This work was funded by the Laboratory Directed Research and Development Program at LLNL under project tracking code 06-SI-002.

---

[1] A. Rousse, C. Rischel, and J.-C. Gauthier, Rev. Mod. Phys. **73**, 17 (2001).

[2] F. Zernike, Science **121**, 345 (1955).

[3] E. Roessl and R. Proksa, Phys. Med. Biol. **52**, 4679 (2007).

[4] D. Attwood, *Soft X-rays and Extreme Ultraviolet Radiation* (Cambridge University Press, Cambridge, CA, 1999).

[5] URL `http://ssrl.slac.stanford.edu/lcls/`.

[6] URL `http://www.xfel.eu/`.

[7] U. Kneissl, H. Pitz, and A. Zilges, Prog. Part. Nucl. Phys. **37**, 349 (1996).

[8] P. Coleman, *Positron beams and their applications* (World Scientific, Singapore, 2000).

[9] H. Weller, M. Ahmed, H. Gao, W. Tornow, Y. Wu, M. Gai, and R. Miskimen, Prog. Part. Nucl. Phys. **62**, 257 (2009).

[10] V. Litvinenko, Nucl. Instr. Phys. Res. A **507**, 527 (2003).

[11] J. Pruet, D. McNabb, C. Hagmann, F. Hartemann, and C. Barty, J. Appl. Phys. **99**, 123102 (2006).

[12] W. Bertozzi, J. Caggiano, W. Hensley, M. Johnson, S. Korbly, R. Ledoux, D. McNabb, E. Norman, W. Park, and G. Warren, Phys. Rev. C **78**, 041601 (2008).

[13] N. Kikuzawa et al., to be published.

[14] S. K. Ride, E. Esarey, and M. Baine, Phys. Rev E **52**, 5425 (1995).

[15] E. Esarey, S. K. Ride, and P. Sprangle, Phys. Rev. E **48**, 3003 (1993).

[16] W. Leemans, R. Schoenlein, P. Volfbeyn, A. Chin, T. Glover, P. Balling, M. Zolotorev, K.-J. Kim, S. Chattopadhyay, and C. Shank, IEEE J. Quantum Electron. **33**, 1925 (1997).

[17] F. Hartemann and A. K. Kerman, Phys. Rev. Lett. **76**, 624 (1996).

[18] F. V. Hartemann, H. A. Baldis, A. K. Kerman, A. L. Foll, J. N. C. Luhmann, and B. Rupp, Phys. Rev. E **64**, 016501 (2001).

[19] F. Hartemann, *High Field Electrodynamics* (CRC Press, Boca Raton, FL, 2002).

[20] F. V. Hartemann, W. J. Brown, D. J. Gibson, S. G. Anderson, A. M. Tremaine, P. T. Springer, A. J. Wootton, E. P. Hartouni, and C. P. J. Barty, Phys. Rev. Spec. Top. - Accel. and Beams **8**, 100702 (2005).

[21] G. Bhatt, H. Grotch, E. Kazes, and D. Owen, Phys. Rev. A **28**, 2195 (1983).

[22] D. Strickland and G. Mourou, Opt. Commun. **56**, 219 (1985).

[23] M. Bowers, S. Burkhart, S. Cohen, G. Erbert, J. Heebner, M. Hermann, and D. Jedlovec, Proc. SPIE **6451**, 1M (2007).

[24] D. J. Gibson, S. G. Anderson, F. V. Hartemann, C. W. Siders, A. M. Tremaine, and C. P. J. Barty, in *Advanced Accelerator Concepts: 12th Workshop*, edited by M. Conde and C. Eyberger (American Institute of Physics, Woodbury, NY, 2006), vol. 877 of *AIP Conference Proceedings*, pp. 602–608.

[25] C. W. Siders, J. L. W. Siders, A. J. Taylor, S.-G. Park, and A. M. Weiner, Appl. Opt. **37**, 5302 (1998).

[26] D. T. Palmer, Ph.D. thesis, Stanford University (1998), (SLAC Technical Report SLAC-R-500).

[27] A. Fukasawa, H. Badakov, B. D. O'Shea, E. Hemsing, J. B. Rosenzweig, and S. G. Anderson, in *Proceedings of the 2007 Particle Accelerator Conference* (IEEE, 2007), pp. 1260–1263.

[28] A. M. Cook, J. B. Rosenzweig, M. Dunning, P. Frigola, and K. Serratto, in *The Physics and Applications of High-Brightness Electron Beams: Proceedings of the 46th Workshop of the INFN ELOISATRON Project*, edited by L. Palumo, J. Rosenzweig, and L. Serafini (World Scientific, 2005), pp. 353–364.

[29] C. Limborg, Z. Li, L. Xiao, J. Schmerge, D. Dowell, S. Gierman, E. Bong, and S. Gilevich, Tech. Rep. LCLS-TN-05-3, Stanford Linear Accelerator Center (2005).

[30] S. G. Anderson and XXXXXX, submitted to Phys. Rev. Spec. Top. - Accel. and Beams. Lawrence Livermore National Laboratory UCRL-JRNL-XXXXXX.

[31] S. C. Fultz, C. L. Whitten, and W. J. Gallagher, IEEE Trans. Nucl. Sci. **18**, 533 (1971).

[32] D. H. Dowell, L. Bentson, R. F. Boyce, S. M. Gierman, J. Hodgson, Z. Li, C. Limborg-Deprey, J. Schmerge, L. Xiao, and N. Yu, in *Proceedings of the 2004 FEL Conference* (2004), pp. 538–541.

[33] S. G. Anderson, J. B. Rosenzweig, G. P. LeSage, and J. K. Crane, Phys. Rev. ST Accel. Beams

5, 014201 (2002).

[34] R. B. Neal, ed., *The Stanford Two-Mile Accelerator* (W. A. Benjamin, 1968).

[35] L. Young and J. Billen, Tech. Rep. LA-UR-96-1835, Los Alamos National Laboratory (1996).

[36] W. J. Brown, S. Anderson, C. P. J. Barty, S. Betts, R. Booth, J. K. Crane, R. R. Cross, D. N. Fittinghoff, D. J. Gibson, F. Hartemann, et al., Phys. Rev. Spec. Topics - Accel. Beams **7**, 060702 (2004).

[37] I. Jovanovic, M. Shverdin, D. Gibson, and C. Brown, Proc. SPIE **6881**, 68810F (2008).

[38] D. J. Gibson, S. G. Anderson, C. P. J. Barty, S. M. Betts, R. Booth, W. J. Brown, J. K. Crane, R. R. Cross, D. N. Fittinghoff, A. M. Tremaine, et al., Phys. Plasmas **11**, 2857 (2004).

[39] M. Berger, J. Hubbell, S. Seltzer, J. Chang, J. Coursey, R. Sukumar, and D. Zucker, *XCOM: Photon Cross Sections Database* (National Institute of Standards and Technology, Gaithersburg, MD, 2005), URL `http://physics.nist.gov/PhysRefData/Xcom/Text/XCOM.html`.

[40] W. J. Brown and F. V. Hartemann, Phys. Rev. Spec. Topics - Accel. Beams **7**, 060703 (2004).

[41] R. Forster et al., NIMB **213**, 82 (2004).

[42] G.Matt, M. Feroci, M. Rapisarda, and E. Costa, Radiat. Phys. Chem. **48**, 403 (????).

[43] N. Pietralla et al., Phys. Rev. Lett. **88**, 012502 (2002).

[44] L. Fagg and S. Hanna, Rev. Mod. Phys. **31**, 711 (1959).

[45] W. Bertozzi, S. Kobly, R. Ledoux, and W. Park, Nucl. Instr. Phys. Res. B **261**, 331 (2007).